mulation in the Basin would be $45 \times 10^{12}$ mol $year^{-1}$ or 0.56 Pg $year^{-1}$. For comparison the Commonwealth Scientific and Industrial Research Organization–GASLAB flask experiment provides independent evidence that the whole of tropical South America may act as a carbon sink, by as much as 2 Pg per year in 1986 to 1987, but not in all years (*19*). Theoretical models of the effects of enhanced storage of carbon in terrestrial biomass as a result of increased $CO_2$ concentrations on net ecosystem fluxes predict a net influx of about 1 Pg $year^{-1}$ for all of the tropics (*20, 21*).

Anthropogenic emissions of $CO_2$ amount to 5.7 Pg of carbon per $year^{-1}$ as fossil fuel burning and about 2 Pg of carbon per year as deforestation (*22, 23*), whereas the annual increase in carbon as atmospheric $CO_2$ is only 3.5 Pg of carbon per year. It is presumed that the difference of about 4.2 Pg of carbon per year is distributed between the oceans and the terrestrial vegetation. Secondary forest, regrowth areas, and plantations are considered to be important candidates for terrestrial sinks (*24, 25*), but the present study suggests that the undisturbed forest may be more important. Year-to-year fluctuations in the carbon balance caused by climatic anomalies may be considerable, contributing to the interannual variation in the rate of $CO_2$ increase (*26*). For example, during 1992 to 1993 when our measurements were being made, the global environment may have been influenced by aerosols from the eruption of Mount Pinatubo, which reduced the solar irradiance by 4% and decreased the temperature by about 0.5°C (*27*). We investigated the sensitivity of the model to changes of this magnitude (Fig. 4). The result suggests great sensitivity to temperature. Part of the accumulated 8.5 mol of carbon per square meter of 1992 to 1993 may have been a result of cooler-than-normal temperatures in that year.

### REFERENCES AND NOTES


1. C. Körner, in *Vegetation Dynamics and Global Change*, A. M. Solomon and H. H. Shugart, Eds. (Chapman & Hall, London, 1993), pp. 53–70.
2. R. M. Gifford, *Aust. J. Plant Physiol.* **21**, 1 (1994).
3. FAO, *Third Interim Report on the State of Tropical Forests* (FAO, Rome, 1992).
4. It is a palm-rich forest, classified as *Floresta Ombrofila Aperta*, with a leaf area index of about 4 and a height of 30 m. There is no evidence of human habitation or logging. The forest is on level terrain with good fetch.
5. R. Leuning and J. B. Moncrieff, *Boundary-Layer Meteorol.* **53**, 63 (1990).
6. A fast-responding closed-path gas analyzer was used to measure $CO_2$ and water vapor concentrations (Li 6262, Li-Cor, Lincoln, NE). Air from above the canopy (53 m above the ground, 20 m above the canopy) was drawn through 6-mm-diameter tubing (Dekabon 1300, Deane, Glasgow, UK) at a flow rate of 4 $dm^3$ $min^{-1}$ into the gas analyzer. The calibration of the analyzer was checked every few days with a calibration cylinder prepared in our laboratory by means of precision gas-mixing pumps (Wosthoff OHG, Bochum, Germany). The vertical component of wind was measured at the same location with a three-dimensional sonic anemometer (A1012R, Gill Instruments, Lymington, UK). Fluxes were calculated as half-hour averages in real time with the software EdiSol, and the results were stored on a laptop computer. Corrections for the nonideal frequency response of the system were subsequently made; we expect the corrected signal to be within 10% of the true flux and to have a negligible zero offset.
7. Over 11 days in the dry season we obtained a mean accumulation rate of 0.09 mol $m^{-2}$ $day^{-1}$ compared with 0.05 mol $m^{-2}$ $day^{-1}$ in the wet season; S. Fan *et al* [*J. Geophys. Res.* **95**, 16851 (1990)] calculated an uptake of 0.05 mol $m^{-2}$ $day^{-1}$ over 50 days at a site near Manaus in central Amazonia.
8. For measurement of $CO_2$ storage in the canopy, vertical profiles were described by fitting spline curves to the $CO_2$ concentrations at 1, 15, 33, and 45 m; numerical integration from ground level to canopy-top gave the carbon stored in the canopy.
9. Mean nocturnal respiration measured from eddy covariance and $CO_2$ storage in the canopy was 6.6 $\mu$mol $m^{-2}$ $s^{-1}$ and did not decline with wind speed, as would be expected if loss due to drainage of cold air is important. The mean obtained independently from chamber methods (20 locations on the soil surface; and plant respiration measured at four heights in the canopy during night) was of similar magnitude, $7.2 \pm 1.0$ $\mu$mol $m^{-2}$ $s^{-1}$.
10. To fit the model, we used a subset of the data: those values obtained when the leaves were dry, the radiation was not fluctuating, and the wind was not from the southern quarter (where the signal may have been contaminated by a river). At 25°C the fitted values were Rubisco activity 68 $\mu$mol $m^{-2}$ $s^{-1}$, canopy electron transport of 130 $\mu$mol $m^{-2}$ $s^{-1}$, and leaf respiration in the dark modeled as 0.7 $\mu$mol $m^{-2}$ $s^{-1}$. The model is fully described in J. Lloyd *et al.*, *Plant Cell Envir.*, in press.
11. S. B. Verma, in *Estimation of Areal Evapotranspiration* (International Association of Hydrological Sciences, Wallingford, UK, 1989).
12. J. Lloyd *et al.*, *Austr. J. Plant Physiol.*, in press.
13. J. Lloyd, *ibid.* **18**, 649 (1991).
14. G. D. Farquhar *et al.*, *Planta* **149**, 78 (1980).
15. P. C. Harley *et al.*, *Oecologia* **70**, 393 (1986).
16. J. Lloyd *et al.*, *Plant Cell Envir.* **15**, 873 (1992).
17. Chambers were sealed to the soil surface, leaf, and stems, and fluxes were related to surface temperatures by an empirical equation.
18. Hourly data are collected with automatic weather stations at several forest towers in Brazil, as part of the Anglo-Brazilian Amazonian Climate Observation Study (ABRACOS) program.
19. I. G. Enting *et al.*, *Tellus* **47B**, 35 (1995).
20. P. J. Polglase and Y. P. Wang, *Aust. J. Bot.* **40**, 641 (1992).
21. J. A. Taylor and J. Lloyd (*ibid.* p. 407) and a recent theoretical study by J. Lloyd and G. D. Farquhar (*Funct. Ecol.*, in press) suggest that tropical forests are currently accumulating carbon in plant and soil at a rate of 5 to 8 mol $m^{-2}$ $year^{-1}$.
22. R. A. Houghton, *Clim. Change* **19**, 99 (1991).
23. U. Siegenthaler and J. L. Sarmiento, *Nature* **365**, 119 (1993).
24. A. E. Lugo and S. Brown, *For. Ecol. Manage.* **54**, 239 (1992).
25. S. C. Wofsy *et al.*, *Science* **260**, 1314 (1993).
26. J. L. Sarmiento, *Nature* **365**, 697 (1993).
27. M. Blumthaler and W. Ambach, *Tellus* **46B**, 76 (1994).


28. We thank W. Coupland, I. Enting, P. Groeneveld, P. G. Jarvis, P. McCracken, A. McWilliam, and C. S. Wong for discussions and for practical help. We thank those organizations in Brazil that facilitated the field work: Instituto Nacional de Colonizacão e Reforma Agraria, Instituto Brasileiro de Meio Ambiente e Recursos Renováveis, Instituto Nacional de Pesquisas Espaciais, and University of Brasilia, Federal University of Rondonia. The ABRACOS project is supported by the UK Overseas Development Administration in collaboration with Agência Brasiliera de Cooperação. The authors acknowledge the financial support provided by the Natural Environment Research Council through its TIGER (Terrestrial Initiative in Global Environment Research) program, award GST/02/605. J.L. was assisted by the Australia/New Zealand/UK Tripartate agreement on climate change.

11 May 1995; accepted 4 August 1995


# Dynamic Contribution to Hemispheric Mean Temperature Trends


John M. Wallace, Yuan Zhang, James A. Renwick



**On the basis of land station data from the Northern Hemisphere, it was determined that roughly half of the temporal variance of monthly mean hemispheric mean anomalies in surface air temperature during the period from 1900 through 1990 were linearly related to the amplitude of a distinctive spatial pattern in which the oceans are anomalously cold and the continents are anomalously warm poleward of 40 degrees north when the hemisphere is warm. Apart from an upward trend since 1975, to which El Niño has contributed, the amplitude time series associated with this pattern resembles seasonally dependent white noise. It is argued that the variability associated with this pattern is dynamically induced and is not necessarily an integral part of the fingerprint of global warming.**


Much of the effort in the monitoring of hemispheric and global temperature trends is focused on the analysis of spatially averaged monthly time series such as the one presented in the top panel of Fig. 1 (*1*). The large month-to-month scatter inherent in such time series tends to obscure whatever interdecadal variability may be present, and it introduces large uncertainties into estimates of the current trends. It can be reduced by temporal smoothing, but only at the expense of the time resolution of the record. Here we show that most of this scatter can be identified with a distinctive spatial pattern of temperature fluctuations that is anchored to the land-sea distribution.


Department of Atmospheric Sciences, Box 351640, University of Washington, Seattle, WA 98195–1640, USA.


In the following, overbars denote spa-

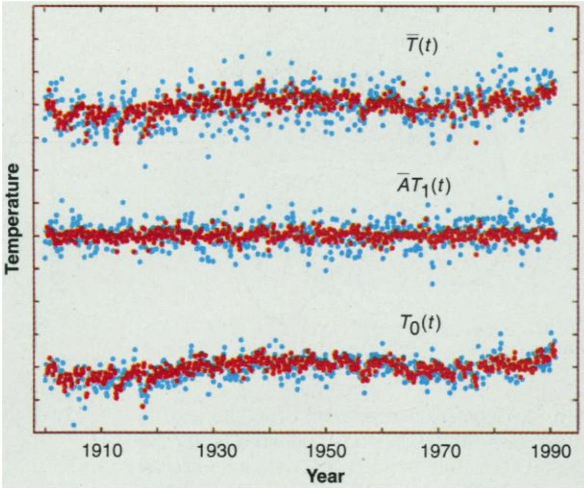


**Fig. 1.** $\bar{T}(t)$ represents monthly mean surface air temperature anomalies averaged over the Northern Hemisphere poleward of 20°N, based on gridded land station data (*1*). Data for cold-season months (November through April) are denoted by blue dots, and data for warm-season months (May through October) are denoted by red dots overprinted on the blue. The reference climatology for defining the anomalies is the period from 1951 through 1980. The fitted time series $\bar{A}T_1(t)$ represents the component associated with the spatial pattern represented in Fig. 3. $T_0(t)$ represents the residual variability in $\bar{T}(t)$. The interval between tick marks on the vertical scale is 1 K.

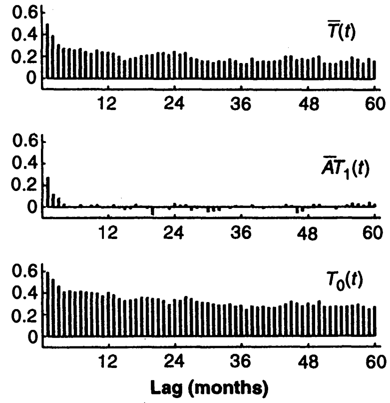


**Fig. 2.** Autocorrelation functions for the time series plotted in Fig. 1 for lag intervals ranging from 1 to 60 months.

tially averaged quantities and asterisks denote departures from spatially averaged quantities: $\overline{(\ )^*} = 0$. The surface air temperature anomaly field $T(x,t)$ is a function of two-dimensional space ($x$) and time ($t$). We seek to identify the spatially varying pattern $A^*(x)$ whose amplitude (or expansion coefficient) time series $T_1(t)$ is maximally correlated with the time series of spatially averaged temperature anomalies $\bar{T}(t)$, subject to the constraint that the spatially averaged value of the pattern be zero. Because this pattern occurs in association with variations in spatially averaged temperature, it is convenient to define $A(x) \equiv A^*(x) + \bar{A}$, of which $\bar{A}$ is the spatially uniform component whose amplitude is also $T_1(t)$. Similarly, $T(x,t) = T^*(x,t) + \bar{T}(t)$, in which $T^*(x,t)$ is composed of the term $A^*(x)T_1(t)$ plus a residual field whose time series at each grid point is uncorrelated with $\bar{T}(t)$.

With these definitions,

$$\bar{T} = T_0 + \bar{A}T_1 \quad (1)$$

where $T_0$ is a residual term that accounts for the unexplained variance of $\bar{T}(t)$. Because $T_1(t)$ is maximally correlated with $\bar{T}(t)$, it follows that $T_0(t)$ and $T_1(t)$ must be uncorrelated:

$$\langle T_0 T_1 \rangle = 0 \quad (2)$$

where $\langle\ \rangle$ refers to a time average. By construction, $T_0(t)$ is linearly uncorrelated with $T^*(x,t)$ at any grid point.

The pattern $A^*$ that occurs in association with $T_1(t)$ can be recovered by formation of the temporal covariance between $\bar{T}(t)$ in Eq. 1 and $T^*(x,t)$ at each individual grid point, which yields

$$\langle \bar{T}(t)T^*(x,t) \rangle \equiv C^*(x) = \langle T_1^{\,2} \rangle \bar{A}\, A^*(x) \quad (3)$$

If we assign A an amplitude by letting $\overline{A^{*2}} = 1$, $A^*(x)$ is simply the spatially normalized form of the covariance pattern $C^*(x)$. Regressing $T^*(x,t)$ onto $A^*(x)$ in the space domain yields

$$T_1(t) = \overline{T^*(x,t)A^*(x)} \quad (4)$$

recalling that $\overline{A^{*2}} = 1$. In effect, the time series $\bar{A}T_1(t)$ represents the least-squares best fit of $\bar{T}(t)$ to the $T^*(x,t)$ field (*2*).

A nondimensional measure of the strength of the pattern compared with the related variations in spatially averaged temperature is $\alpha \equiv (\overline{A^{*2}})^{1/2}/\bar{A} = 1/\bar{A}$.

The formalism described above was applied to monthly mean, gridded surface air temperature anomalies over the Northern Hemisphere poleward of 20°N that were based on land station data (*1*), with each grid point being weighted in proportion to its area (*3*). The fitted and residual time series $\bar{A}T_1(t)$ and $T_0(t)$ are displayed in the middle and lower panels of Fig. 1, and their autocorrelation functions are shown in Fig. 2. It is evident that $T_1(t)$, which accounts for 46% of the variance of $\bar{T}(t)$, exhibits little autocorrelation at time lags beyond a month or two. The visually coherent features in $\bar{T}(t)$, including most of the warming since the mid-1970s, are mirrored in the residual, $T_0(t)$, which exhibits stronger autocorrelation than does $\bar{T}(t)$ at lags beyond 5 years. The cold-season data exhibit larger month-to-month scatter, particularly in $\bar{T}(t)$ and $\bar{A}T_1(t)$.

$A/\bar{A}$ (Fig. 3) is positive over the high-latitude continents, reaching values in excess of 4 over the Yukon and much of Siberia, and is predominantly negative over the North Atlantic and over the continents equatorward of 40°N. The pattern strength $\alpha$ is 1.8. In order to obtain a more complete representation of the spatial pattern associated with $T_1(t)$, we related it to the lower tropospheric temperature field (*4*), for which coverage is available over the oceans as well as the continents. The regression of this field upon $\bar{A}T_1(t)$ (Fig. 4) indicates that months with above-normal $T_1$ tend to be characterized by anomalously cold oceans and warm continents poleward of 40°N (*5*).

The data points in the monthly time series in Fig. 1 were partitioned into cold- and warm-season time series (denoted by superscripts c and w), averaged by 6-month season, and smoothed with a 5-year running mean filter to produce the plots in Fig. 5. It is evident that the smoothed $\bar{T}^c$ and $\bar{T}^w$ differ by as much as 0.3 K within short segments of the record: $\bar{T}^c$ exhibits substantially more variability on time scales ranging from 3 to 10 years. Particularly notable in this respect is the apparent upward trend in $\bar{T}^c$ from the late 1970s onward, which is mirrored in $T_1^{\,c}$. Apart from a slight upward trend in $T_0^{\,c}$ relative to $T_0^{\,w}$, the smoothed time series $T_0(t)$ exhibits remarkably little seasonality over the 90-year period of record, particularly after 1950 when the data are more reliable. Because $\bar{A}T_1^{\,w}(t)$ exhibits so little variability during the warm season, it follows that on time scales of years or longer, $\bar{T}^w(t)$ closely resembles $T_0(t)$.

$T_0(t)$ and $T_1(t)$ in Eq. 1 should not be

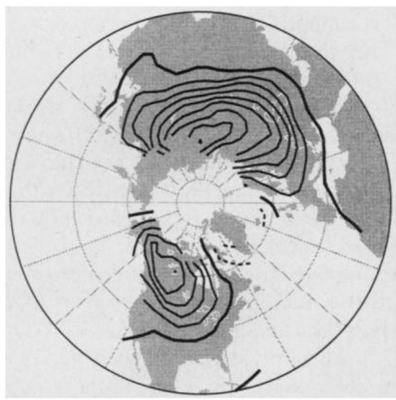

**Fig. 3.** The spatial pattern $A/\bar{A} = 1 + A^*/\bar{A}$, obtained by regressing $\bar{A}T_1(t)$ (Fig. 1) upon gridded surface air temperature (*12*). Contour interval is 1 K per degree Kelvin, the zero contour is thickened, and negative contours are dashed.

viewed as amplitudes of natural modes of variability of the temperature field in the same sense as principal component time series. Their physical significance derives not from their formal definition but from their contrasting frequency dependence (Figs. 1 and 2), their contrasting seasonality (Figs. 1 and 5), the distinctive shape of $A^*(x)$ in relation to the underlying land-sea distribution (Figs. 3 and 4), and the fact that virtually the same cold ocean–warm land (hereafter referred to as COWL) pattern is recovered for $A^*(x)$ in an analysis of the hemispheric mean lower tropospheric temperature field, which includes both land and ocean (6).

The strong linear correlation between the amplitude of this COWL pattern and hemispheric mean temperature is a consequence of the fact that land surfaces, with their small heat capacities, equilibrate much more rapidly with the temperature of the overlying air mass than does sea surface temperature. Hence they experience larger temperature variability in response to month-to-month changes in atmospheric circulation patterns, which is reflected in the overlying surface air temperature. It follows that hemispheric mean surface air temperature is largely determined by the temperature of the continents, even when surface air temperature over the oceans is taken into account in the averaging.

Variations in hemispheric mean temperature associated with the COWL pattern, as manifested in the term $\bar{A}T_1(t)$ in Eq. 1, are dynamically induced in the sense that they occur in response to the changing configuration of warm and cold air masses relative to the underlying land-ocean distribution. The residual term $T_0(t)$ may be regarded as an estimate of the radiatively induced component of the variability. The fact that the frequency spectrum of $\bar{A}T_1(t)$ is so much whiter than that of $T_0(t)$ and the variability of $\bar{A}T_1(t)$ is so much larger during the cold season (the season of strong air mass contrasts) supports this interpretation.

The changes in $\bar{T}$, $T_0$, and $\bar{A}T_1$ from the reference period from 1951 through 1980 to the decade from 1981 through 1990 are summarized in Table 1. The rise in $T_0$ was nearly the same for the warm and cold seasons and was about two-thirds as large as that in $\bar{T}$ reported in (7). The reported accelerated winter and spring warming over the high-latitude continents since the mid-1970s (7) shows up in our analysis as the upward trend $\bar{A}T_1^{\,c}(t)$ in Fig. 5. The prevalence of positive regression coefficients of $T^c(x,t)$ upon $A^*(x)$ from the mid-1970s onward, which is also evident in the lower tropospheric temperature field (6), reflects the juxtaposition of regional climate anomalies in various sectors of the hemisphere. The prevalence of

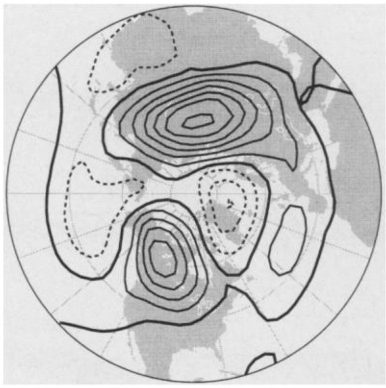

**Fig. 4.** Regression coefficient of $\bar{A}T_1(t)$ (Fig. 1) upon lower tropospheric temperature (4) for the period from 1946 through 1990. Contour interval is 1 K per degree Kelvin, the zero contour is thickened, and negative contours are dashed.

the warm phase of the El Niño–Southern Oscillation (ENSO) cycle, together with persistent negative sea surface temperature anomalies over the extratropical central North Pacific, accounts for much, if not all, of the anomalous warmth over Alaska and western Canada and the relative coolness over the North Pacific (8); and the prevalence of the high index phase of the North Atlantic Oscillation (9) has contributed to the warmth of northern Europe and the coolness of the subpolar North Atlantic.

The COWL pattern contains elements of the greenhouse warming fingerprint (10). Hence, it is not clear whether the coincidence of these regional anomalies that contributed to the prevalence of the positive polarity of the COWL pattern during the past 15 years should be regarded as part of the fingerprint, or whether it is largely fortuitous. If an amplified wintertime warming over the high-latitude continents were indeed an integral part of the signature or fingerprint of interdecadal-to-century variability of Northern Hemisphere surface air temperature, it is not clear why $\bar{A}T_1(t)$ picks up so little of the interdecadal-to-century–scale temperature variability, though perhaps it could be argued that the warming of the past 15 years is occurring for different reasons than did the variability that preceded it. Nor is it clear how a high-latitude continental radiative forcing or a rather modest rise in $T_0$ could exert such a strong influence on the ENSO cycle as well as on regional circulation patterns over the Atlantic and Pacific sectors. And unless the variability associated with $T_1(t)$ is clearly understood to be an integral part of the fingerprint of greenhouse warming, it is questionable whether it should be included in assessments of hemispheric or global mean temperature trends; it might be more appropriate to deal with it as a separate issue.

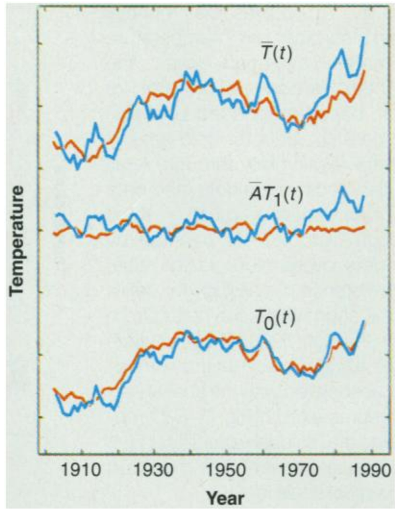


**Fig. 5.** Data are shown as in Fig. 1, but the time series are partitioned into the contributions from cold- and warm-season months (denoted by blue and red, respectively) and smoothed. The interval between tick marks on the vertical scale is 0.5 K.

**Table 1.** Rises in hemispheric mean (poleward of 20°N) surface air temperature, based on land station data (1) from the reference period from 1951 through 1980 to the decade from 1981 through 1990 in degrees Kelvin.

| | All calendar months | Cold season | Warm season |
|---|---|---|---|
| $\bar{T}(t)$ | 0.32 | 0.44 | 0.20 |
| $\bar{A}T_1(t)$ | 0.13 | 0.24 | 0.02 |
| $T_0(t)$ | 0.19 | 0.20 | 0.18 |

Our interpretation of $T_0(t)$ as an estimate of the radiatively induced variability in hemispheric mean temperature should not be regarded as implying that the temperature changes induced by changing concentrations of aerosols, trace gases, and the distribution of cloud cover are devoid of spatial structure. The analysis strategy described here is capable of resolving only one spatial pattern, which turns out to be the COWL pattern. If the radiatively induced variability were known to exhibit a preferred pattern or fingerprint that could be specified independently of the analysis (for example, on the basis of general circulation model experiments), it might be possible to adapt the analysis strategy to take it into account. However, in view of the multiplicity of atmospheric constituents that contribute to the radiative forcing, each with its own peculiar space-time structure that includes both seasonal and secular variations (11), it would be surprising if any single spatial pattern could account for an appreciable fraction of the radiatively induced variance of hemispheric mean temperature over the past century.

## REFERENCES AND NOTES


1. The series is based on the gridded monthly mean data set compiled under the sponsorship of the U.S. Department of Energy, as described in P. D. Jones *et al.*, *J. Clim. Appl. Meteorol.* **25**, 161 (1986) and updated in the references in (*7*).
2. Because this procedure maximizes the squared temporal covariance between $T^*(x,t)$ and $\bar{T}(t)$, it is equivalent to performing singular value decomposition analysis, as outlined in C. S. Bretherton, C. Smith, J. M. Wallace, *J. Clim.* **5**, 541 (1992), where $T^*(x,t)$ is the left field and $\bar{T}$ is the one-dimensional right field. If the number of spatial degrees of freedom in $T^*(x,t)$ is too large in comparison with the number of independent samples, this procedure will tend to overfit $\bar{T}(t)$, yielding an intricate pattern $A^*$ that would not be reproducible in an independent data set [for example, see R. E. Davis, *J. Phys. Oceanogr.* **8**, 233 (1978)]. We investigated the sensitivity of $T_1(t)$ to the number of degrees of freedom in $A^*(x)$. Following T. P. Barnett and R. Preisendorfer [*Mon. Weather Rev.* **115**, 1825 (1987)], we expanded the $T^*$ field in terms of its own empirical orthogonal functions, and we fit the $N$ leading associated expansion coefficient time series to $\bar{T}(t)$ by the method of least squares. Within the range $N = 5$ to 10, $T_1(t)$ and $A^*(x)$ closely resemble those shown in the text, and the fraction of the variance of $\bar{T}(t)$ explained by the fit is also quite comparable. Hence, because of the spatial autocorrelation inherent in the $T^*$ field, the effective number of spatial degrees of freedom in this particular application is only on the order of 5 to 10, so overfitting is not a problem.
3. The data are formatted on a latitude-longitude grid, so grid point values must be weighted by cosine of latitude in estimation of $\bar{T}(t)$ and computation of $T_1(t)$ from (*4*).
4. The field represented in Fig. 4 is the thickness of the layer between the 1000- and 500-hectopascal (or millibar) pressure surfaces, which is directly proportional to the mean temperature (in degrees Kelvin) of the intervening layer, which extends from the earth's surface up to a height of ~5.5 km above sea level. Gridded analyses of these fields have been produced by the National Oceanic and Atmospheric Administration (NOAA) National Meteorological Center on a daily or twice-daily basis since 1946, in support of operational numerical weather prediction.
5. If the hemispheric lower tropospheric temperature field is regressed upon $\bar{T}(t)$ instead of $T_1(t)$, the pattern is similar but biased toward positive values. A similar but somewhat weaker pattern is obtained when the lower tropospheric temperature field is regressed upon the time series of hemispheric mean lower tropospheric temperature, averaged over the area poleward of 40°N, including both land and ocean (*6*).
6. J. M. Wallace, Y. Zhang, L. Bajuk, *J. Clim.*, in press.
7. C. K. Folland, T. R. Karl, K. Ya. Vinnikov, in *Climate Change: The IPCC Scientific Assessment*, J. T. Houghton, G. J. Jenkins, J. J. Ephraums, Eds. (Cambridge Univ. Press, 1990), pp. 195–238; C. K. Folland *et al.*, in *Climate Change 1992: The Supplementary Report to the IPCC Scientific Assessment*, J. T. Houghton, B. A. Callander, S. K. Varney, Eds. (Cambridge Univ. Press, 1992), pp. 135–170; D. E. Parker, P. D. Jones, C. K. Folland, A. Bevan, *J. Geophys. Res.* **99D**, 14373 (1994).
8. K. E. Trenberth, *Bull. Am. Meteorol. Soc.* **71**, 988 (1990); ______and J. W. Hurrell, *Clim. Dyn.* (in press); C. Deser and M. L. Blackmon, *J. Clim.* **6**, 1743 (1993); N. E. Graham, *Clim. Dyn.* **10**, 135 (1994); ______ T. P. Barnett, R. Wilde, M. Ponafer, S. Schubert, *J. Clin.* **7**, 1416 (1994); Y. Zhang, J. M. Wallace, N. Iwasaka, *ibid.*, in press; M. Latif and T. P. Barnett, *Science* **266**, 634 (1994); A. Kumar, A. Leetmaa, M. Ji, *ibid.*, p. 632.
9. J. W. Hurrell, *Science* **269**, 676 (1995).
10. T. M. L. Wigley and T. P. Barnett, in *Climate Change: The IPCC Scientific Assessment*, J. T. Houghton, G. J. Jenkins, J. J. Ephraums, Eds. (Cambridge Univ. Press, Cambridge, 1990), pp. 239–256, T. P. Barnett, M. E. Schlesinger, X. Jiang, in *Greenhouse Gas–Induced Climatic Change: A Critical Appraisal of Simulations and Observations*, M. E. Schlesinger, Ed. (Elsevier, Amsterdam, 1991), pp. 559–568; K. Hasselmann, *J. Clim.* **6**, 1957 (1993), B. D. Santer, T. M. L. Wigley, P. D. Jones, *Clim. Dyn.* **9**, 265 (1993).
11. See, for example, R. J. Charlson and T. M. Wigley, *Sci. Am.* **270**, 48 (1994).
12. Regression of $T(x,t)$ upon $\bar{A}T_1(t)$ yields $\bar{A}\langle TT_1\rangle/\bar{A}^2\langle T_1^2\rangle$. From Eq. 1, $\bar{A}^2\langle T_1^2\rangle = \bar{A}\langle \bar{T}T_1\rangle$. Hence, the regression coefficient is equivalent to $\langle TT_1\rangle/\langle \bar{T}\bar{T}T_1\rangle$, which reduces to $A/\bar{A}$.


13. We thank E. Sarachik, T. N. Palmer, I. Blade, C. B. Leovy, and an anonymous reviewer for reading an earlier version of the manuscript and offering helpful suggestions. Supported by NSF's Climate Dynamics Program under grant ATM 9215512 and by the NOAA Office of Global Programs.

13 June 1995; accepted 24 August 1995


# On the Origins of Spontaneous Polarization in Tilted Smectic Liquid Crystals

Demetri J. Photinos and Edward T. Samulski*

**The rapid electrooptic response of ferroelectric liquid crystals—stratified (smectic) melts exhibiting spontaneous electric polarization—makes them candidates for the next generation of electrooptic shutters and liquid crystal displays. The model advanced here suggests that polarity is indigenous to tilted smectics and that spontaneous polarization derives from the packing constraints mesogens experience, a tilt-dependent correlation of molecular conformation with orientation. First-rank orientational order parameters ($C_{xx}$) are nonzero with a tilt- (temperature-) dependent magnitude, and under certain packing conditions, the sign of $C_{xx}$ varies with tilt. These results have a direct bearing on experimental observations because most ferroelectric liquid crystals exhibit a tilt-dependent spontaneous polarization and some show an inversion of the sign of the polarization.**

Spontaneous polarization is the signature and defining characteristic of certain smectic phases called ferroelectric liquid crystals (FLCs). Since Meyer's seminal announcement that ferroelectricity can be realized in tilted smectics composed of chiral mesogens (*1*), it has been generally accepted that FLC attributes revolve around the subtle interplay between electric dipoles and molecular chirality (*2*). However, in modeling of idealized mesogens confined to lamellae, we found an indigenous polarity in even the simplest representation of a tilted smectic phase, one that was independent of mesogen molecular structural details (such as dipole moments and chirality). More than 20 years ago, Priest anticipated such a possibility in a formal description of the smectic-C ($S_C$) phase using the tensor components of the molecular mean field (*3*). Our modeling has led us to conclude (i) that spontaneous polarization originates from a statistical biasing of mesogen configurations that derives from steric interactions in stratified, tilted smectics and (ii) that its temperature dependence, including the observed inversion of the sign of the polarization in certain FLCs, is simply a consequence of molecular packing considerations.

The molecules forming the $S_C$ phase typically consist of an elongated, aromatic (mesogenic) core linked to flexible, aliphatic chains ("tails") at both of its ends (**I** and **II** in Table 1). Because of molecular flexibility, the molecular symmetry is understood in the statistical or time-averaged sense. There is spatial segregation in the $S_C$ phase along the smectic layer normal $Z$: core-rich zones alternate with chain-rich ones (Fig. 1). A chiral center in the mesogen (**II**) results in an incompletely averaged electric dipole component $\mu_\perp$ transverse to the mesogenic core that contributes to an electric polarization along the $C_2$ axis ($X$ axis) of the tilted phase: $P_X \propto \Sigma\mu_\perp$. Meyer and his co-workers used symmetry arguments suggesting that chirality and transverse dipoles are sufficient to give rise to ferroelectricity (*1*), but these arguments do not permit the evaluation of the polarization $P_X$ because they do not refer to any particular mechanism by which the polar order develops. Several such mechanisms have been proposed over the last two decades, but all of them invoke ad hoc constraints or parameters to affect polarization. These include a binding-site model that biases rotations of a chiral mesogen's "zig-zag" contour, thereby generating a nonzero $\mu_\perp$ (*4*), weighted mesogen conformational statistics that manufacture a temperature-dependent polarization of variable sign (*5*), and a model with multiple transverse molecular axes circumscribed to mimic different degrees of biased mesogen rotation (*6*). This report demonstrates that a generic representation of a statistically twofold-symmetric mesogen (for example, an idealization of the apolar, achiral mesogen **I**) together with the ordering constraints imposed on it by the $S_C$ phase give rise to nonzero, first-rank polar order parameters.

Figure 2, A and B, illustrates two dispositions of a flexible primitive mesogen—a three-segment representation of the real mesogen—confined within a smectic layer. Both dispositions are compatible with strat-

D. J. Photinos, Department of Physics, University of Patras, Patras 26100, Greece.
E. T. Samulski, Department of Chemistry, University of North Carolina, Chapel Hill, NC 27599–3290.

*To whom correspondence should be addressed.